

# Theory of Coherent Raman Superradiance Imaging of Condensed Bose Gases

H. Uys and P. Meystre

*Department of Physics*

*The University of Arizona, Tucson, AZ, 85721*

We model the off-resonant superradiant Raman scattering of light from a cigar-shaped atomic Bose-Einstein condensate. Absorption images of transmitted light serve as a direct probe of long range coherence in the condensate. Our multimode theory is in good agreement with the time-dependent spatial features observed in recent experiments, and the inclusion of quantum fluctuations in the initial stages of the superradiant emission accounts well for shot-to-shot fluctuations.

## I. INTRODUCTION

In recent work, L.E. Sadler *et al.* discuss the use of superradiant Raman scattering as a probe of long range coherence in an ultra-cold bosonic gas [1]. Their investigation is one of few experimental studies of extended sample superradiance that is not only temporally, but also spatially resolved.

Superradiance is a well-known phenomenon [2] that was first discussed by Dicke [3] in 1954. In that process, atoms scatter light collectively, producing a short burst of intense radiation. In a typical superradiance experiment with Bose-Einstein condensates, an elongated sample of ultracold atoms is subjected to a pump pulse of far off-resonant laser light. For an appropriate polarization of that field, the cigar-shaped condensate geometry results in the scattering of photons predominantly into modes propagating along the long axis of the sample, commonly referred to as the end-fire-modes (EFM). As the atomic cloud is Bose-condensed, the scattering process simultaneously leads to the coherent amplification of the recoiling atomic fields. Such coherent matter-wave amplification (CMA) has been observed both in the case of Rayleigh scattering [4, 5, 6] and of Raman scattering [7, 8], and several theoretical descriptions of this effect have been published [9, 10, 11, 12].

A necessary condition for superradiance to occur is [13, 14, 15]

$$\tau_c \ll T_2^*, \quad (1)$$

where  $T_2^*$  is the reciprocal inhomogeneous linewidth and  $\tau_c = 2/(c\rho\gamma\lambda^2)^{1/2}$  is the superradiant cooperation time with  $\rho$  the atomic density,  $c$  the speed of light,  $\lambda$  the wavelength and  $\gamma$  the linewidth of an isolated atom.

An ultracold Bosonic gas at temperature  $T$  with  $0 < T < T_c$ , where  $T_c$  is the critical temperature, consists of both condensed and non-condensed phases. As Doppler broadening for the two phases can be dramatically different, it is possible for the appropriate choice of experimental parameters to have condition Eq. (1) satisfied for the condensed phase, but not the non-condensed phase [4]. Under such circumstances light will scatter superradiantly only from the condensed portion of the gas, thus providing the experimenter with a sensitive probe of that phase. In Ref. [1] this approach is followed to

both quantify the condensate number and study the spatial and temporal evolution of the superradiant process. It provides a novel probe of long-range coherence which may lead to insight in the symmetry-breaking dynamics of normal- to superfluid phase transitions. To our knowledge only one previous study [4] exists that resolves spatial features in extended sample superradiance in atomic vapors. In that case the angular pattern of the emitted EFM was integrated over the course of a superradiant pulse and found to consist of several bright spots (Fig. 3(a) in Ref. [4]).

Zobay and Nikolopoulos [16, 17] have given a detailed semiclassical analysis of the spatial features of both the matter-wave and the optical fields in CMA experiments based on Rayleigh scattering. They found that propagation effects play a crucial role in the amplification process and account for several characteristic features seen in experiments [4, 7]. These include the characteristic “X” and fan shapes of the atomic recoil modes corresponding to the strong and weak pulse limits respectively, the asymmetry between forward and backward side-modes in the strong pulse regime, and the depletion of the condensate center in the weak pulse regime. Furthermore, they found that low superradiant emission does not necessarily imply a small EFM field inside the atomic sample, as a result of the scattering of EFM photons back into the pump beam. They also demonstrated that propagation effects lead to sub-exponential growth of the scattered fields in contrast to the exponential growth seen in fully quantized uniform field models, an effect reminiscent of laser lethargy in short-wavelength optical amplifiers [18, 19].

An important aspect of superradiance experiments is the appearance of large shot-to-shot fluctuations, a result of the quantum noise that dominates the dynamics during the initial stages of the experiment [2, 20, 21, 22]. At later times the scattered fields become macroscopically occupied and evolve in an essentially classical manner from initial conditions determined by those quantum fluctuations. A common strategy to treat the full evolution of superradiance is therefore to break the problem into an initial quantum stage followed by a classical stage. The initial stage is analyzed primarily to determine the appropriate probability distribution of initial conditions for the classical stage. Experimentally observed fluctuations in the classical stage are simulated by solving the dynamics a large number of times with initial conditions

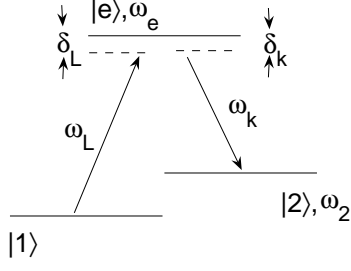


FIG. 1: Three-level Raman transition

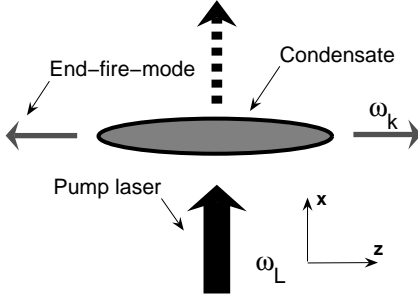


FIG. 2: Experimental setup.

chosen according to this probability distribution, each simulation representing a single realization of the experiment.

The primary aim of this paper is to provide a detailed model to complement the experiments reported in Ref. [1]. We generalize the semiclassical model of Refs. [16, 17] to the Raman scattering case, and extend it to a multimode quantum description that allows for a systematic treatment of the build-up of the classical fields from quantum noise, thereby accounting for shot-to-shot fluctuations. Whereas Refs. [16, 17] focussed on the post-pump expansion patterns of the recoiling modes to check self-consistency of their predictions, we investigate the time-dependent imaging of the condensate *while* undergoing superradiant emission. We find good qualitative agreement with experimental observations.

The paper is organized as follows. Section II discusses the experiment under consideration, introduces our model, and considers the initial stages of the evolution of the atoms and light field, treating the scattered optical field quantum mechanically. Section III turns then to the classical stage by solving coupled Maxwell-

Schrödinger equations within the slowly varying envelope approximation. Numerical results are presented in Sec. IV, and Sec. V is a summary and conclusion.

## II. INITIAL STAGE AND QUANTUM FLUCTUATIONS

We consider a cigar-shaped Bose-Einstein condensate of width  $w$  and length  $L$  with a total of  $N$  atoms. The ultra-cold atoms in the condensate undergo Raman scattering between two ground states  $|1\rangle$  and  $|2\rangle$  via an off-resonant excited state  $|e\rangle$ . The energy of level  $|1\rangle$  is taken as the zero of energy, and the energies of the states  $|2\rangle$  and  $|e\rangle$  are  $\hbar\omega_2$  and  $\hbar\omega_e$ , respectively, see Fig. 1. We assume that the transition  $|1\rangle \rightarrow |e\rangle$  is driven by a classical pump laser  $\mathbf{E}_L(t)$  of frequency  $\omega_L$  and polarized along the  $\hat{y}$ -axis, see Fig. 2, with

$$\omega_L = \omega_e - \delta_L \quad (2)$$

while the transition  $|e\rangle \rightarrow |2\rangle$  takes place via spontaneous emission to a continuum of vacuum modes with frequencies

$$\omega_k = \omega_e - \omega_2 - \delta_k. \quad (3)$$

The total electric field is then

$$\begin{aligned} \hat{\mathbf{E}} &= \mathbf{E}_L(t) + \sum_{\hat{\epsilon}} \int d\mathbf{k} \hat{\mathbf{E}}_{\mathbf{k}} \\ &= \hat{\mathbf{y}} \left[ E_L(t) e^{i(\mathbf{k}_L \cdot \mathbf{r} - \omega_L t)} + E_L^*(t) e^{-i(\mathbf{k}_L \cdot \mathbf{r} - \omega_L t)} \right] \\ &\quad + \sum_{\hat{\epsilon}} \int d\mathbf{k} \left[ \left( \frac{\hbar\omega_{\mathbf{k}}}{2\epsilon_0 V} \right)^{\frac{1}{2}} \hat{\epsilon}_{\mathbf{k}} \hat{a}_{\hat{\epsilon}\mathbf{k}}(t) e^{i\mathbf{k} \cdot \mathbf{r}} + h.c. \right], \end{aligned}$$

where the creation operators  $\hat{a}_{\hat{\epsilon}\mathbf{k}}^\dagger(t)$  obey the usual bosonic commutation relations

$$[\hat{a}_{\hat{\epsilon}\mathbf{k}}, \hat{a}_{\hat{\epsilon}'\mathbf{k}'}^\dagger] = \delta(\mathbf{k} - \mathbf{k}') \delta_{\hat{\epsilon}\hat{\epsilon}'}. \quad (4)$$

The incident laser field envelope  $E_L(t)$  is taken as constant in amplitude during the initial stages of the amplification process, but its full time dependence can be accounted for in the classical stages of the evolution.

We proceed by introducing bosonic matter-field creation and annihilation operators  $\hat{\psi}_i^\dagger(\mathbf{r}, t)$ ,  $(\hat{\psi}_i(\mathbf{r}, t))$ , that create (annihilate) an atom at position  $\mathbf{r}$  in electronic state  $|i\rangle = |1\rangle, |e\rangle$  or  $|2\rangle$ , with

$$[\hat{\psi}_i(\mathbf{r}, t), \hat{\psi}_j^\dagger(\mathbf{r}', t)] = \delta_{ij} \delta(\mathbf{r} - \mathbf{r}'), \quad (5)$$

in terms of which the Hamiltonian of the atom-field system is  $\hat{H} = \hat{H}_0 + \hat{H}_c$ , with

$$\hat{H}_0 = \sum_{\mathbf{k}} \int d\mathbf{r} \hbar\omega(\mathbf{k}) \hat{a}_{\mathbf{k}}^\dagger(t) \hat{a}_{\mathbf{k}}(t) + \int d\mathbf{r} \left\{ \hbar\omega_e \hat{\psi}_e^\dagger(\mathbf{r}, t) \hat{\psi}_e(\mathbf{r}, t) + \hbar\omega_2 \hat{\psi}_2^\dagger(\mathbf{r}, t) \hat{\psi}_2(\mathbf{r}, t) \right\}, \quad (6)$$

---

and the interaction Hamiltonian

---

$$\hat{H}_c = - \int d\mathbf{r} \left\{ \hat{\mathbf{E}} \cdot \left[ \mathbf{d}_1 \hat{\psi}_e^\dagger(\mathbf{r}, t) \hat{\psi}_1(\mathbf{r}, t) + \mathbf{d}_2 \hat{\psi}_e^\dagger(\mathbf{r}, t) \hat{\psi}_2(\mathbf{r}, t) \right] + h.c. \right\}, \quad (7)$$


---

describes the electric dipole interaction between the atoms and the electromagnetic field,  $\mathbf{d}_i$  being the dipole moment of the  $|i\rangle \leftrightarrow |e\rangle$  transition.

We assume that the atoms are initially in their ground state  $|1\rangle$ , and that the pump laser is sufficiently far detuned from resonance for the excited state population to remain negligible at all times. The excited level  $|e\rangle$  can then be adiabatically eliminated in the standard fashion. Thus transforming to slowly varying interaction picture operators

$$\tilde{a}_{\mathbf{k}}(\mathbf{r}, t) = \hat{a}_{\mathbf{k}} e^{i\omega_L t} \quad (8)$$

and performing the rotating wave approximation (RWA), yields the effective Hamiltonian

$$\tilde{H}_c = - \int d\mathbf{r} \int d\mathbf{k} \left\{ g(\mathbf{k}) \tilde{a}_{\mathbf{k}}^\dagger \tilde{\psi}_2^\dagger(\mathbf{r}, t) e^{i(\mathbf{k}_L - \mathbf{k}) \cdot \mathbf{r}} \tilde{\psi}_1(\mathbf{r}, t) e^{i(\delta_L - \delta_k)t} + h.c. \right\}, \quad (12)$$


---

where

$$g(\mathbf{k}) = (\hat{\mathbf{y}} \cdot \mathbf{d}_1)(\hat{\mathbf{e}} \cdot \mathbf{d}_2) \sqrt{\frac{\omega_k}{2\hbar\epsilon_0 V}} \left( \frac{\delta_k + \delta_L}{\delta_k \delta_L} \right) E_L. \quad (13)$$

In Eq. (12) we have neglected higher-order scattering terms coupling modes of the scattered light field, an approximation justified in the early stages.

The effect of the Hamiltonian  $\tilde{H}$  is to transfer atoms initially in the ground state  $|1\rangle$  and with spatial wave function  $\phi_0(\mathbf{r})$  into the ground state  $|2\rangle$  with a momentum-conserving spatial wave function  $\phi_0(\mathbf{r}) e^{i(\mathbf{k}_L - \mathbf{k}) \cdot \mathbf{r}}$  via scattering of a photon into mode  $\mathbf{k}$ . Following Ref. [10] we therefore expand the matter-field operators into quasi-modes according to

$$\tilde{\psi}_1(\mathbf{r}) = \phi_0(\mathbf{r}) \tilde{c}_0 \quad (14)$$

and

$$\tilde{\psi}_2(\mathbf{r}) = \int d\mathbf{q} \phi_0(\mathbf{r}) e^{i\mathbf{q} \cdot \mathbf{r}} \tilde{c}_q, \quad (15)$$

where  $\tilde{c}_0$  annihilates a particle in a quasi-mode with electronic state  $|1\rangle$  and wave function  $\langle \mathbf{r} | 0 \rangle = \phi_0(\mathbf{r})$  and  $\tilde{c}_q$  annihilates a particle in a quasi-mode with electronic state  $|2\rangle$  and wave function  $\langle \mathbf{r} | \mathbf{q} \rangle = \phi_0(\mathbf{r}) e^{i\mathbf{q} \cdot \mathbf{r}}$ . These quasi-modes are nearly orthogonal provided that they are separated by an angle

$$\theta_\perp \gtrsim 2K_w/|k| = \lambda/(\pi w),$$

where  $K_w = 2/w$  is the momentum width of the condensate. In that case the quasi-mode creation and annihilation operators  $\tilde{c}_q$  obey to a good approximation bosonic commutation relations

$$[\tilde{c}_q, \tilde{c}_{q'}^\dagger] \approx \delta_{qq'} \quad (16)$$

and are statistically independent during the early stages of the evolution.

In terms of the quasi-modes  $q$ , the Hamiltonian (12) becomes

$$H_c = \sum_{\mathbf{q}} \int d\mathbf{k} \left\{ \eta(\mathbf{k}, q) e^{i(\delta_L - \delta_k)t} \tilde{a}_{\mathbf{k}}^\dagger \tilde{c}_q^\dagger \hat{c}_0 + h.c. \right\} \quad (17)$$

where

$$\eta_{\mathbf{q}}(\mathbf{k}) = g(\mathbf{k}) \int d\mathbf{r} |\phi_0(\mathbf{r})|^2 e^{i(\mathbf{k}_L - \mathbf{k} - \mathbf{q}) \cdot \mathbf{r}}. \quad (18)$$

We have used the normalization condition  $\int d\mathbf{r} |\phi_0(\mathbf{r})|^2 = 1$ . The Hamiltonian (17) differs from the effective Hamiltonian derived by Moore and Meystre for the Rayleigh scattering case [10] in that the electronic state of recoiling atomic modes is  $|2\rangle$  instead of the original ground state  $|1\rangle$  and the term oscillating with frequency  $\delta_L - \delta_k = \omega_k - (\omega_L - \omega_2)$  enforces the coupling of the scattered modes to photons with frequency  $\omega_L - \omega_2$  instead of  $\omega_L$ .

With these differences in mind, we may easily generalize the results of Ref. [10] and determine that the quasi-modes initially grow exponentially,

$$\tilde{c}_{\mathbf{q}} = \exp[G_{\mathbf{q}} N t / 2] \tilde{c}_{\mathbf{q}}(0) + \int_0^t d\tau \exp[G_{\mathbf{q}} N t / 2] \tilde{f}_{\mathbf{q}}^\dagger(t - \tau), \quad (19)$$

where

$$G_{\mathbf{q}} = 2\pi \int d\mathbf{k} |\eta_{\mathbf{q}}(\mathbf{k})|^2 \delta[\omega_k - (\omega_L - \omega_2)] \quad (20)$$

and  $\tilde{f}_{\mathbf{q}}^\dagger(t - \tau)$  is a noise operator the second-order correlation functions of which are given in the Markov approximation by

$$\langle \tilde{f}_{\mathbf{q}}^\dagger(t) \tilde{f}_{\mathbf{q}}(t') \rangle = 0, \quad (21)$$

$$\langle \tilde{f}_{\mathbf{q}}(t) \tilde{f}_{\mathbf{q}}^\dagger(t') \rangle = G_{\mathbf{q}} N \delta(t - t'). \quad (22)$$

In this limit, the probability  $P_{\mathbf{q}}(n, t)$  of having  $n$  atoms in mode  $\mathbf{q}$  at time  $t$  is that of a chaotic field,

$$P_{\mathbf{q}}(n, t) = \frac{1}{\bar{n}_{\mathbf{q}}(t)} \left( 1 + \frac{1}{\bar{n}_{\mathbf{q}}(t)} \right)^{-(n+1)}, \quad (23)$$

where  $\bar{n}_{\mathbf{q}}(t) = \langle \tilde{c}_{\mathbf{q}}^\dagger \tilde{c}_{\mathbf{q}} \rangle$  is the mean number of atoms in the quasi-mode  $\mathbf{q}$  at time  $t$ .

An important feature of the linear gain factor  $G_{\mathbf{q}}$  is that it remains relatively constant for quasi-modes excited via the scattering of photons at small angles  $\theta_{\mathbf{k}}$  with respect to the long axis of the condensate. This is the case until  $\theta_{\mathbf{k}}$  reaches the geometric angle

$$\theta_g \approx \frac{w}{L}$$

after which the linear gain  $G_{\mathbf{q}}$  falls off rapidly. The electromagnetic modes corresponding to scattering into that angle collectively form the EFMs, and they dominate the short-time dynamics of the system.

This suggests that we may accurately simulate the linear dynamics of the superradiant system by considering the scattering of photons into a finite number of modes distributed within a solid angle  $2\pi\theta_g$  around the long axis of the condensate only. We note that while the geometric angle into which significant scattering takes place is fixed by the aspect ratio of the condensate, the number  $m$  of independent quasi-modes depends also on the wavelength of the optical fields involved,

$$m \approx \left( \frac{\theta_g}{\theta_\perp} \right)^2 = \left( \frac{\pi w^2}{2\lambda L} \right)^2 = F^2, \quad (24)$$

where  $F$  is the Fresnel number. Typical experiments correspond to a number of quasi-modes  $m \approx 1 \sim 10^2$ .

### III. CLASSICAL EVOLUTION

We now turn to the quantum-noise initiated classical regime that occurs once the superradiance process is fully underway and the scattered modes are macroscopically occupied. In typical experiments of Ref. [1] the velocity of the recoiling atoms is such that they may traverse half a condensate width over the course of a single run of the experiment. In addition, atom-atom scattering may cause significant dephasing on the same time scale. In this section we therefore include both kinetic energy and mean field atom-atom collisional terms.

In the classical regime the optical field can be described by a complex field amplitude

$$\begin{aligned} \mathbf{E}_{cl} &= \mathbf{E}_L + \sum_{\mathbf{k}} \mathbf{E}_{\mathbf{k}} \\ &= \hat{\mathbf{y}} \left[ E_L(\mathbf{r}, t) e^{i(\mathbf{k}_L \cdot \mathbf{r} - \omega_L t)} + E_L^*(\mathbf{r}, t) e^{-i(\mathbf{k}_L \cdot \mathbf{r} - \omega_L t)} \right] \\ &\quad + \sum_{\mathbf{k}} \hat{\mathbf{e}} \left[ E_{\mathbf{k}}(\mathbf{r}, t) e^{i(\mathbf{k} \cdot \mathbf{r} - \omega_k t)} + E_{\mathbf{k}}^*(\mathbf{r}, t) e^{-i(\mathbf{k} \cdot \mathbf{r} - \omega_k t)} \right]. \end{aligned}$$

Following the discussion of Sec. II we restrict the sum over  $\mathbf{k}$  to the discrete set of quasi-modes in the end-fire cone and set  $\omega_k = \omega_L - \omega_2$ . At this point we no longer assume that the pump field remains undepleted. As usual, the field amplitudes  $E_i(\mathbf{r}, t)$  are assumed to be slowly varying,

$$|\nabla E_i(\mathbf{r}, t)| \ll |k_i E_i(\mathbf{r}, t)|, \quad (25)$$

$$\left| \frac{\partial E_i(\mathbf{r}, t)}{\partial t} \right| \ll |\omega_i E_i(\mathbf{r}, t)|. \quad (26)$$

Eliminating adiabatically the excited electronic state of the atoms as before by introducing the slowly varying Schrödinger field operators

$$\tilde{\psi}_0(\mathbf{r}, t) = \hat{\psi}_1(\mathbf{r}, t) \quad (27)$$

$$\tilde{\psi}_{\mathbf{k}_L}(\mathbf{r}, t) = \hat{\psi}_e(\mathbf{r}, t) e^{i(\omega_e + \omega_{er})t} e^{-i\mathbf{k}_L \cdot \mathbf{r}} \quad (28)$$

$$\tilde{\psi}_{\mathbf{k}}(\mathbf{r}, t) = \hat{\psi}_{\mathbf{k}}(\mathbf{r}, t) e^{i(\omega_2 + \omega_{2r})t} e^{-i(\mathbf{k}_L \cdot \mathbf{r} - \mathbf{k} \cdot \mathbf{r})}, \quad (29)$$

where  $\hbar\omega_{er} = \hbar^2 k_L^2 / 2m$  and  $\hbar\omega_{2r} = \hbar^2 (k_L^2 + k^2) / 2m$ , results in the effective Hamiltonian  $\tilde{H} = \tilde{H}_0 + \tilde{H}_{aa} + \tilde{H}_c$  where

$$\tilde{H}_0 = - \int d\mathbf{r} \left\{ \sum_{\mathbf{k}} \frac{\hbar^2}{2m} \tilde{\psi}_{\mathbf{k}}^\dagger \nabla^2 \tilde{\psi}_{\mathbf{k}} \right\}, \quad (30)$$

$$\tilde{H}_{aa} = - \int d\mathbf{r} \left\{ U_{11} \tilde{\psi}_0^\dagger \tilde{\psi}_0^\dagger \tilde{\psi}_0 \tilde{\psi}_0 + \sum_{\mathbf{k}} \left( U_{kk} \tilde{\psi}_{\mathbf{k}}^\dagger \tilde{\psi}_{\mathbf{k}}^\dagger \tilde{\psi}_{\mathbf{k}} \tilde{\psi}_{\mathbf{k}} + U_{1k} \tilde{\psi}_0^\dagger \tilde{\psi}_{\mathbf{k}}^\dagger \tilde{\psi}_{\mathbf{k}} \tilde{\psi}_0 \right) \right\}, \quad (31)$$

$$\tilde{H}_c = - \int d\mathbf{r} \sum_{ij} \frac{g_{ij}}{(1 - i\gamma/\delta_L)} \tilde{\psi}_i^\dagger(\mathbf{r}, t) \tilde{\psi}_j(\mathbf{r}, t). \quad (32)$$

Here

$$g_{ij} = \frac{d_i d_j}{3\delta_L \hbar} E_i^*(\mathbf{r}, t) E_j(\mathbf{r}, t), \quad (33)$$

in which the factor 3 arises from an average over all possible orientations of the dipole and

$$U_{11(kk)} = \frac{4\pi\hbar^2 a}{m}, U_{1k} = \frac{8\pi\hbar^2}{m} (a + ika^2), \quad (34)$$

where  $a$  is the s-wave scattering length and the indices  $i, j$  run over  $-k, 0, k$ . The last term on the right in Eq. (34)

is a momentum-dependent loss that has been used to account for elastic scattering losses in the Gross-Pitaevski equation [23]. It arises upon keeping the second-order term when expanding the manybody T-matrix in powers of  $k$ . For the Raman system under consideration we need not include higher-order modes of the form  $\tilde{\psi}_{n\mathbf{k}_L+q\mathbf{k}}$  ( $n, q$  being integers) in the sum over  $\mathbf{k}$ , since the second ground state can no longer absorb pump photons [7].

Within the slowly varying envelope approximation (SVEA) the Hamiltonian (32) yields the matter-wave Heisenberg equations of motion

$$\frac{d\Psi_0(\mathbf{r}, t)}{d\tau} = \frac{i}{(1 - i\gamma/\delta_L)} \mathcal{E}_L^* \left[ \frac{d_1}{d_2} \mathcal{E}_L \Psi_0 + \sum_{\mathbf{k}} \mathcal{E}_{\mathbf{k}} \Psi_{-\mathbf{k}} \right] + i \sum_j u_{1j} |\Psi_j|^2 \Psi_0 \quad (35)$$

$$\frac{d\Psi_{\mathbf{k}}(\mathbf{r}, t)}{d\tau} = -\kappa \cdot \nabla \Psi_{\mathbf{k}} + \frac{i}{(1 - i\gamma/\delta_L)} \mathcal{E}_{-\mathbf{k}}^* \left[ \mathcal{E}_L \Psi_0 + \frac{d_2}{d_1} \sum_{\mathbf{k}} \mathcal{E}_{\mathbf{k}} \Psi_{-\mathbf{k}} \right] + i \sum_j u_{kj} |\Psi_j|^2 \Psi_{\mathbf{k}}. \quad (36)$$

We have cast these equations in dimensionless units where the dimensionless time is

$$\tau = \frac{\Omega_L^2}{\delta_L} t, \quad (37)$$

in which

$$\Omega_L = \frac{dE_L^{\text{in}}}{\sqrt{3}\hbar} \quad (38)$$

is the the Rabi frequency of the incident laser field of amplitude  $E_L^{\text{in}}$  and  $d = \sqrt{d_1 d_2}$ . The electric field amplitudes are rescaled as

$$\mathcal{E}_i = \frac{E_i}{E_L^{\text{in}}}, \quad (39)$$

and the matter-wave fields as

$$\Psi_i = \frac{\tilde{\psi}_i}{\sqrt{\rho_c}}, \quad (40)$$

where

$$\rho_c = \frac{N}{Lw^2} \quad (41)$$

is a characteristic density.

When performing the derivatives of the kinetic energy term, dimensional analysis along with the SVEA indicate that the second order derivative is smaller than the first by a factor  $10^{-4}$ . We have therefore retained only the advective contribution (first term on the right in Eq. (36)) with a dimensionless velocity

$$\kappa = \frac{\delta_L}{L\Omega_L^2} \frac{\hbar}{2m} (\mathbf{k}_L + \mathbf{k}). \quad (42)$$

Finally, the rescaled atom-atom scattering strength is

$$u_{ij} = \frac{\delta_L}{\Omega_L^2} U_{ij}. \quad (43)$$

The factor  $\gamma/\delta_L$  in Eqs. (35) and (36) is due to the inclusion of a phenomenological decay term to account for losses due to spontaneous emission from the excited state.

The evolution of the optical field is governed by the Maxwell wave equation coupled to the macroscopic polarization of the condensate. Treating the pump laser as a continuous wave we find

$$\frac{\partial \mathcal{E}_L}{\partial \xi} = \frac{i\aleph}{(1 - i\gamma/\delta_L)} \Psi_0^\dagger \left\{ \frac{d_1}{d_2} \mathcal{E}_L \Psi_0 + \sum_k \mathcal{E}_k \Psi_{-k} \right\} \quad (44)$$

$$\text{sign}(k) \frac{\partial \mathcal{E}_k}{\partial \zeta} = \frac{i\aleph}{(1 - i\gamma/\delta_L)} \Psi_{-k}^\dagger \left\{ \mathcal{E}_L \Psi_0 + \frac{d_2}{d_1} \sum_k \mathcal{E}_k \Psi_{-k} \right\} \quad (45)$$

where  $\xi = x/L$ ,  $\zeta = z/L$  and

$$\aleph = \frac{\pi d^2 \rho_c}{3 \epsilon_0 \hbar \delta_L} \frac{L}{\lambda}. \quad (46)$$

Equations (44) and (45), together with Eqs. (35) and (36), fully describe the multimode dynamics of the slowly varying envelopes of the electric and matter-wave fields. They may be solved analytically in the short-time regime as shown in Appendix A. In this regime the fields  $\Psi_{\pm k}$  obey

$$\Psi_k(\mathbf{r}, \tau) = \psi_{k'}(0) I_0 \left( 2\sqrt{\tau \Delta} \right), \quad (47)$$

where  $\psi_{k'}(0)$  is the square root of the recoiling mode density at  $\tau = 0$  and  $\Delta$  is a function of  $\zeta$  defined in Appendix A. A similar result was previously obtained in Ref. [17].

#### IV. NUMERICAL RESULTS

##### A. General considerations

This section presents selected results from numerical simulations of the onset and growth of superradiant scattering in a cigar-shaped condensate. We assume here that all atoms in the condensate at temperature  $T = 0$  are initially in the electronic ground state  $|1\rangle$ , and approximate their center-of-mass wave function by a separable Thomas-Fermi profile (in dimensionless units),

$$\Psi_0(\mathcal{R}) = 6^{3/2} L^2 / w^2 \prod_i \sqrt{(\mathcal{L}_i / 2L)^2 - \mathcal{R}_i^2}$$

where the product is over the rescaled spatial coordinates  $\mathcal{R}_i$  and  $\mathcal{L}_i$  is the corresponding condensate width [26]. Close to the Thomas-Fermi radii, where the Thomas-Fermi approximation breaks down, we let the wavefunction go to zero smoothly by matching both the function and its derivative to a Gaussian tail. This is necessary to prevent numerical instabilities resulting from the advective term in Eq. (36). To remain true to the experiments of Ref. [1], we choose the aspect ratio of the condensate to be  $w/L \approx 0.1$ .

As we have seen, the amplitudes of the end-fire modes at the onset of the classical regime are stochastic variables the values of which must be selected at random

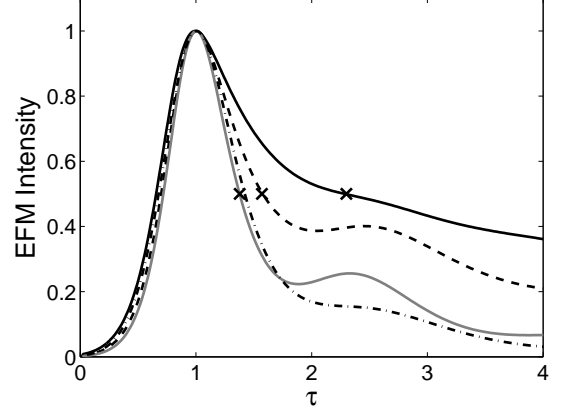


FIG. 3: Typical time evolution of the EFM intensity. These simulations neglect dissipation, mean-field interactions and effects due to photon recoil. The curves correspond to: solid line  $\aleph = 6.0$ , dashed line  $\aleph = 3.0$ , gray line  $\aleph = 1.0$  and dot-dashed line  $\aleph = 1.0$  with  $\gamma/\delta_L = 0.04$ . The x's mark points at which the spatial field and absorption profiles are plotted in Figs. 4-6.

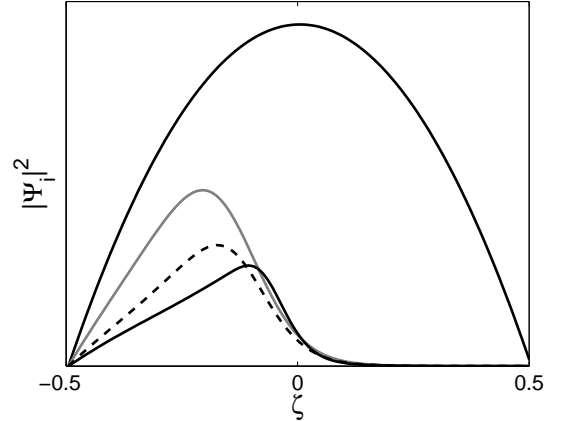


FIG. 4: Density profile of the condensate at  $\tau = 0$  (top solid line) and of the atomic side mode  $\Psi_{+k}$  at half the maximum EFM intensity, as indicated by x's in Fig. 3: solid line  $\aleph = 6.0$ , dashed line  $\aleph = 3.0$  and gray line  $\aleph = 1.0$ . Mean-field interactions, dissipation and effects due to photon recoil are neglected.

from run-to-run consistently with the results of Sec. II. However, to set the stage for our discussion, we consider first a simplified situation with only one left-recoiling and one right-recoiling side-mode of equal initial amplitudes small compared to the amplitude of  $\Psi_0$ , but with the same spatial structure. We include, for the moment, only the atom-light coupling and neglect the mean-field interaction, photon recoil and dissipation.

Figure 3 illustrates examples of superradiant EFM pulse shapes, for different values of the atom-field cou-

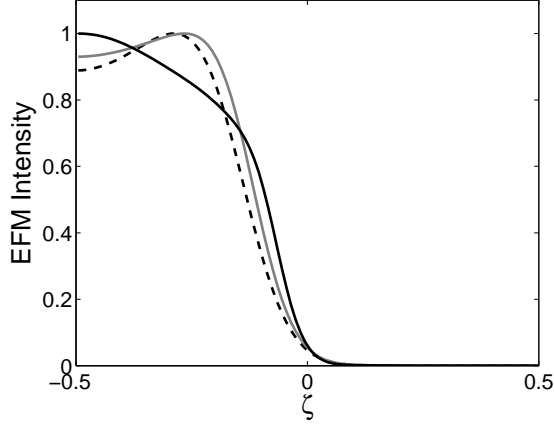


FIG. 5: Typical spatial envelopes of EFM electric fields at half maximum EFM intensity as indicated by x's in Fig. 3: solid line  $\aleph = 6.0$ , dashed line  $\aleph = 3.0$ , gray line  $\aleph = 1.0$ . The peak in intensity for  $\aleph = 1.0$  and  $3.0$  arises due to scattering of EFM photons back into the probe beam. Mean-field interactions, dissipation and effects due to photon recoil are neglected here.

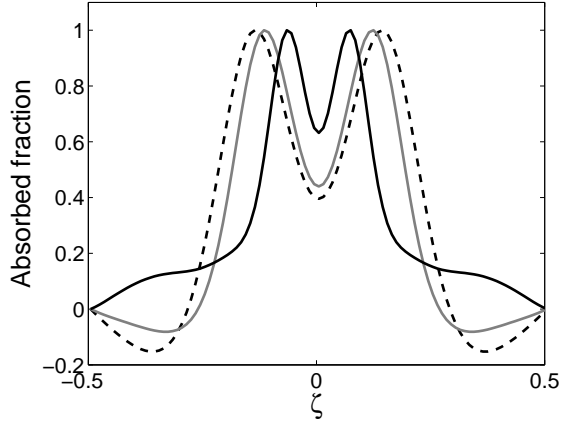


FIG. 6: Absorption profile of the pump pulse along the  $z$  axis at half maximum EFM intensity as indicated by x's in Fig. 3: solid line  $\aleph = 6.0$ , dashed line  $\aleph = 3.0$  and gray line  $\aleph = 1.0$ . Mean-field interactions, dissipation and effects due to photon recoil are neglected here.

pling strength  $\aleph$ . To facilitate comparison we scaled the peak intensities to 1, and the time axes so that the peaks coincide. The gray line, corresponding to  $\aleph = 1.0$ , demonstrates a typical main pulse followed by a secondary peak, an effect known as ringing [2]. Increasing the coupling strength to  $\aleph = 3.0$  raises the secondary peak maximum relative to the first peak, as shown by the dashed line. The black line, for which  $\aleph = 6.0$ , represents a qualitatively different regime: The superradiant maximum is now followed by a slowly decaying tail rather than ringing. Dissipation also leads to suppression of the ringing, as shown by the dot-dashed line which is

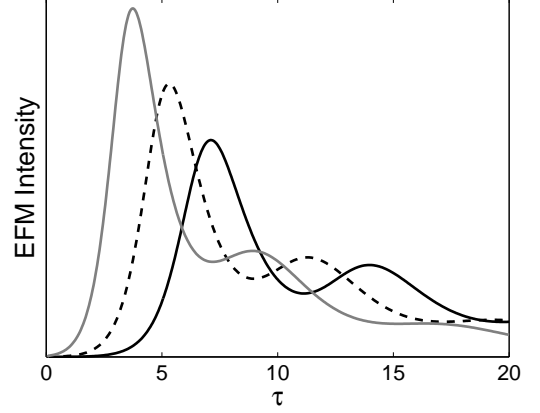


FIG. 7: Time evolution of EFM intensity for an initial density of the recoiling modes  $10^{-6}$  (solid black line),  $10^{-5}$  (dashed line) and  $10^{-4}$  (gray line) times smaller than the condensate density.

for  $\gamma/\delta_L = 0.04$  and  $\aleph = 1.0$ . The appearance of ringing with increased coupling strength has been observed experimentally, Fig. 3(b) of Ref. [4].

Figures 4 and 5 show spatial profiles along the long axis  $z$  of the condensate, of the atomic side mode  $\Psi_{+k}$  and of the corresponding EFM field  $\mathcal{E}_{-k}$ . Here the same values of  $\aleph$  as in Fig. 3 were used: solid line  $\aleph = 6.0$ , dashed line  $\aleph = 3.0$  and gray line  $\aleph = 1.0$ . The EFM profiles have again been scaled for comparison. All  $z$ -axis profiles correspond to the times indicated by the x's in Fig. 3. In Fig. 4 the atomic mode  $\Psi_{+k}$  grows from the left edge of  $|\Psi_0|(\zeta)^2$ , a consequence of the build-up of the EFM electric field as it moves across the condensate, see Fig. 5. For clarity the mode  $\Psi_{-k}$  is not shown. It is simply a mirror image of  $\Psi_{+k}$ . Interestingly, in the absence of dissipation the weaker coupling strength is more efficient at scattering atoms to ground state  $|2\rangle$  over a single superradiant pulse, as evidenced by the gray line in Fig. 4. Keep in mind, however, that the time scale is slower for the weaker coupling, a feature not apparent due to the scaling of time in the figure.

For the cases  $\aleph = 1.0$  and  $3.0$ , the EFM profile peaks before reaching the edge of the condensate, see Fig. 5. During the dynamical evolution this peak appears shortly after the first intensity maximum in Fig. 3. It is a consequence of the EFM field being scattered back into the probe beam from atoms in ground state  $|2\rangle$ . As pointed out in Ref. [17] this may cause a strong EFM field to exist within the atomic system despite small emission outside the sample.

The fraction of absorbed laser intensity

$$A(x, z) = \frac{|\mathcal{E}_L^{\text{in}}|^2 - |\mathcal{E}_L(x, z)|^2}{|\mathcal{E}_L^{\text{in}}|^2} \quad (48)$$

is shown in Fig. 6 for  $x \gg w$  after the laser field exits the condensate, again for the same values of  $\aleph$  as in Fig. 3

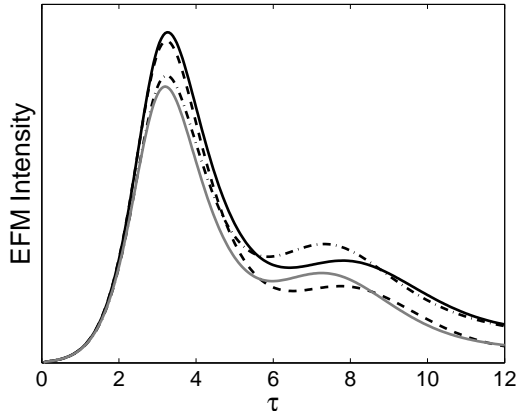


FIG. 8: Comparison of EFM intensity with  $\gamma/\delta_L = 8 \times 10^{-3}$ ,  $\aleph = 1.7$  for superradiance only (black solid line), superradiance and photon recoil (dashed line), superradiance and mean-field interaction (dot-dashed line), and superradiance with both mean-field interactions and photon recoil included (gray line).

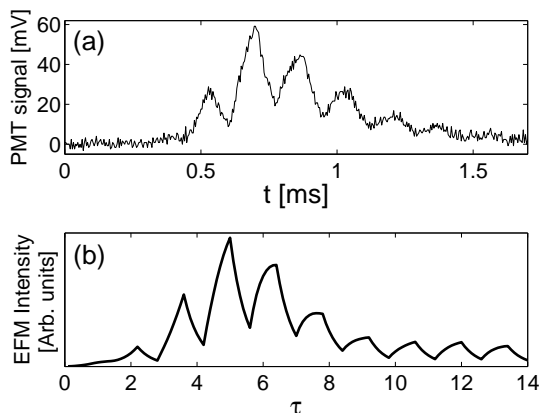


FIG. 9: Comparison of (a) experimental photomultiplier signal of EFM intensity to, see [1], (b) a theoretical simulation with  $\aleph = 1.7$ . Experimental data by D. Stamper-Kurn *et al.* [24].

and at half the EFM intensity maximum. The two central peaks in each absorption profile appear close to the edges of the condensate early in the time evolution and migrate towards each other. Secondary features, such as regions of gain around the edges of the condensate, appear shortly after the EFM pulse maximum for  $\aleph = 1.0$  and  $3.0$ . This gain is a signature indicating that EFM light is being scattered back into the pump field. For  $\aleph = 6.0$  the growth of secondary absorption peaks at the edges of the condensate, as shown by the black line, is the dominant secondary feature rather than gain.

The semi-classical model is valid provided the relevant modes are macroscopically occupied. In the above simu-

lations the initial seed amplitude of the recoiling atomic modes was treated as a free parameter that may in general be chosen to fit experimental data. To study the effects of this choice of initial amplitude we plot in Fig. 7 the time evolution of EFM intensity for initial densities of the recoiling modes being respectively  $10^{-6}$  (solid black line),  $10^{-5}$  (dashed line) and  $10^{-4}$  (gray line) times smaller than the condensate density. For smaller initial amplitude the time to peak superradiance is delayed and the ringing peak is higher relative to the intensity maximum.

Now consider the effects of mean-field interactions and photon recoil. Figure 8 shows the time evolution of the EFM intensity for  $\gamma/\delta_L = 8 \times 10^{-3}$  and  $\aleph = 1.7$ . The results are for simulations taking into account superradiance only (solid black line), superradiance and recoil velocity (dashed line), superradiance and mean-field interaction (dot-dashed line), and superradiance with both mean-field interactions and recoil velocity (gray line). The recoil velocity was so chosen that an atom would traverse roughly half a condensate width over  $\Delta\tau = 12.0$ . The primary effect of including the photon recoil and mean-field interactions is to reduce the EFM amplitude. Note that the height of the ringing peak is increased somewhat relative to the first intensity maximum when including only mean-field interactions. But generally speaking we do not find significant qualitative changes in the spatial and temporal evolution of either matter or light fields other than a reduction in overall amplitudes and slight relative delays.

## B. Comparison with experiment

The primary purpose of the multimode treatment is to describe the quantum fluctuations that govern the initial evolution of the system. As discussed in Sec. II this entails randomly choosing seed amplitudes for the initial state of the recoiling atomic modes with the appropriate statistical properties. We have found, however, that the multimode description gives the same results as a single-mode model as far as EFM intensity and absorption profiles are concerned, provided that the sum of initial seed densities in the multimode case is equal to the seed density of the single-mode system. For a single run of the experiment a single-mode description is therefore sufficient if the seed densities are chosen judiciously. We thus turn to a comparison of the single-mode theory to data obtained in experiments at UC Berkeley [24].

As described in Ref. [1], a Bose condensate of  $N = 1.6 \times 10^6$   $^{87}\text{Rb}$  atoms trapped in an Ioffe-Pritchard trap with trap frequencies of  $\omega_{x,y,z} = 2\pi(48, 48, 5)s^{-1}$  was superradiantly pumped via the  $F = 1 \rightarrow F' = 1$  D1 transition from the  $|F = 1, m_f = -1\rangle$  to the  $|F = 2, m_f = 1\rangle$  groundstates via a sequence of ten pump pulses of  $100 \mu\text{s}$ , each separated by a  $68 \mu\text{s}$  delay. Fig. 9(a) shows a typical EFM pulse sequence recorded on a photomultiplier tube (PMT). The rise time between pulses is a consequence of



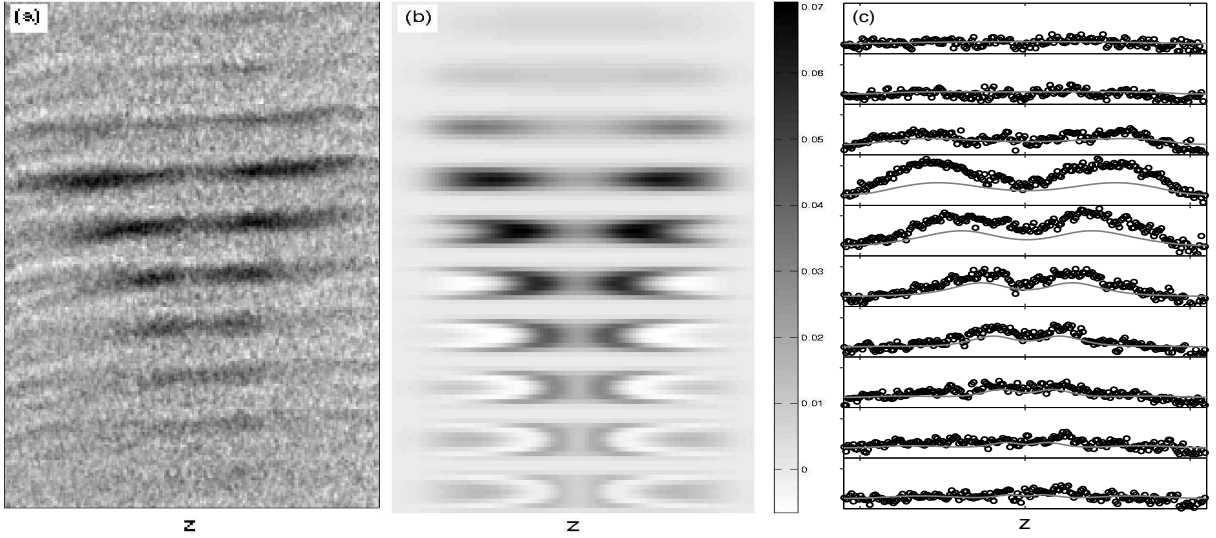


FIG. 10: (a) Experimental coherent absorption imaging data, see [1], in which darkest regions indicate strongest absorption, with a maximum absorption of  $\sim 15\%$ . (b) Simulated absorption images for  $\aleph = 1.7$  and an initial density of recoiling modes  $|\Psi_0|^2/10^4$ . (c) Comparison of experimental (circles) to simulated (gray lines) transverse averaged absorption profiles. The maximum in the experimental data is  $\sim 6\%$ . In all figures time evolves from top to bottom and the horizontal frame width is  $L \approx 200\mu\text{m}$ . Experimental data by D. Stamper-Kurn *et al.* [24].

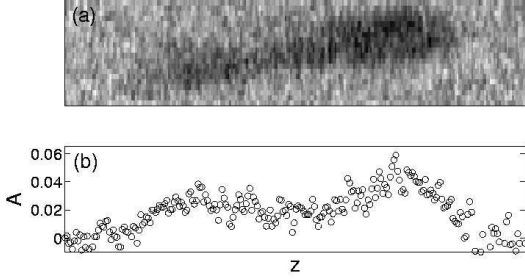


FIG. 11: Example of (a) Typical absorption image, see [1], and (b) its averaged profile, demonstrating asymmetry that may arise from quantum fluctuations. Experimental data by D. Stamper-Kurn *et al.* [24].

the slow response time of the PMT. The lack of ringing indicates that dissipation plays a significant role in the dynamics. Dissipation due to spontaneous emission may be estimated using  $\gamma/\delta_L = \omega^3 d^2 / 3\pi\epsilon_0 \hbar c^3 \delta_L \approx 8 \times 10^{-3}$  [25]. Given an  $s$ -wave scattering length for  $^{87}\text{Rb}$  of  $a \approx 10^2 a_0$  where  $a_0$  is the Bohr radius, we find  $\aleph \approx 1.7$ . The experimental data agree qualitatively with the three dimensional simulation, see Fig. 9(b). Here the initial density of recoiling atoms was chosen  $10^4$  times smaller than the condensate density, and the dimensionless time scale was such that an atom would traverse roughly half a condensate width over the course of the pulse sequence as in the Berkeley experiments. The PMT response was accounted for by convoluting the EFM intensity with a response function with response time of the order of the pulse separation.

Experimental absorption images corresponding to the PMT signal of Fig. 9(a) are shown in Fig. 10(a), where time evolves from top to bottom and each image is the time averaged absorption over the duration of each pulse in the sequence. Consistently with the observation that in this experimental run the asymmetry in the absorption profile is small, we have taken the initial amplitudes of the atomic side modes  $\Psi_{\pm k}$  to be equal. The resulting absorption images are shown in Fig. 10(b). An effect not resolved in Ref. [1] is the weak absorption seen at the upper- and lower edges of the condensate in the lower six images of Fig. 10(b). This absorption arises since the edges of the condensate are less dense than the center, thus delaying superradiance in time and intensity. A comparison of our simulation to transverse averaged experimental absorption profiles is shown in Fig. 10(c). The qualitative agreement is quite satisfactory although the value of the peak absorption is underestimated by a factor of  $\sim 2$ . Note that the averaging procedure suppresses gain and other secondary features seen in the simulation of Fig. 10(b), thus leading to the simple double peaked structure of Fig. 10(c). The simulation furthermore suggests that these features are too small in spatial extent and amplitude to be resolved in the experimental data. We emphasize that the only free parameters in this simulation are the initial seed amplitude and the total time duration of the pulse sequence. They are tightly constrained by, respectively, the rise time to peak superradiance relative to the EFM pulse width and the EFM pulse width relative to the overall time duration of the pulse sequence.

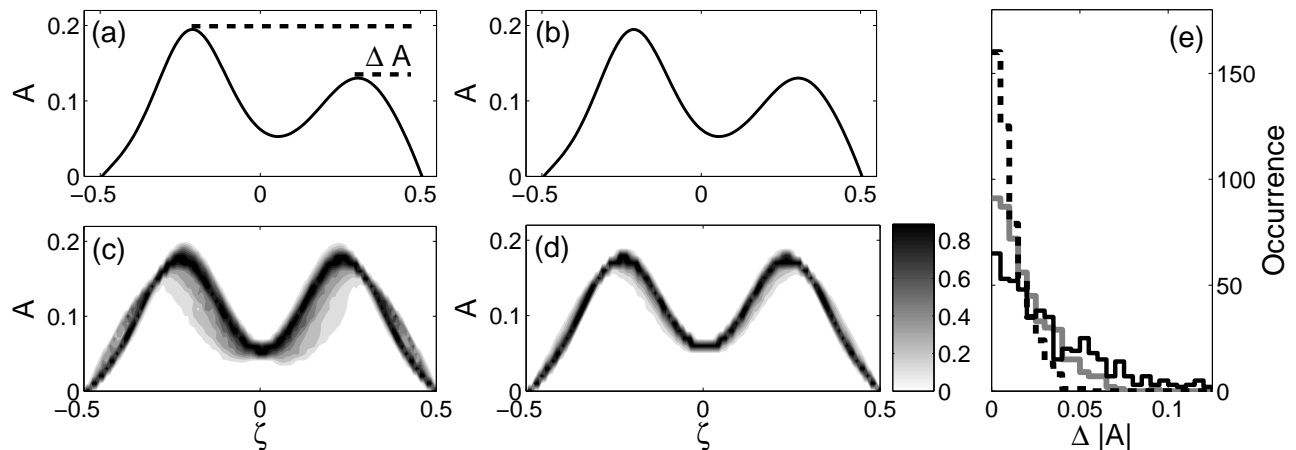


FIG. 12: Absorption profile  $A(z)$  of the input laser field. Figures (a)-(b) are representative profiles resulting from single realizations of a superradiance experiment for geometries with (a)  $m = 5$  and (b)  $m = 20$  quasi-modes each in the left- and right EFM directions. The peak separation,  $\Delta\alpha$ , as indicated by the dotted lines in (a) characterizes the asymmetry. Figures (c) and (d) give the frequency of occurrence of the absorption profiles resulting from 500 realizations for (c)  $m = 5$  and (d)  $m = 20$ . As indicated by the gray scale in the color bar, the darkest shade of gray corresponds to the most frequent occurrences. (e) Distribution of the asymmetry of absorption peaks from 500 realizations, for systems with  $m = 5$  (black line),  $m = 10$  (gray line) and  $m = 20$  (dashed line) quasi-modes in both the left- and right EFM directions.

### C. Shot-to-shot fluctuations

We now turn to the shot-to-shot fluctuations resulting from the quantum noise-dominated early stages of the emission process. In Fig. 11(a) we show a typical absorption image obtained experimentally and exhibiting strong asymmetry, as well as its transverse averaged profile in Fig. 11(b). To account for this asymmetry we solve the multimode Eqs. (35)-(36) and (44)-(45) for  $\aleph = 3.0$ , neglecting mean-field interactions and effects due to photon recoil, with the initial amplitude of each quasi-mode chosen from the probability distribution (23) independently of the other modes. The average particle number  $\bar{n}_{\mathbf{q}}$  is taken to be the same for all distributions.

Figures 12(a)-(b) show absorption profiles for two randomly chosen realizations of a superradiance experiment for systems with (a)  $m = 5$  and (b)  $m = 20$  quasi-modes each in the left- and right EFM directions of propagation. In all cases the absorption profile is shown at the time of the first EFM intensity maximum in either the left- or right traveling EFM. The separation  $\Delta A$ , as indicated by the dotted lines in (a), may be used to characterize the asymmetry. Figure 12(c)-(d) shows a gray scale plot constructed from 500 realizations of the superradiance experiment for (c)  $m = 5$  and (d)  $m = 20$  quasi-modes each in the left- and right travelling EFMs. Each profile is again taken at the first EFM intensity maximum. The gray scale represents the frequency of occurrence of absorption, with darkest shade of gray being the highest frequency.

The distribution of absorption asymmetries,  $\Delta A$ , for a

random set of 500 realizations of the experiment is plotted in Fig. 12(e) for  $m = 5$  (black line),  $m = 10$  (gray line) and  $m = 20$  (dashed line) quasi-modes each in the left- and right EFM directions. As may be expected the width of the distribution decreases with increasing number of modes.

## V. CONCLUSION

We have presented a multimode model of Raman superradiance scattering to explain recent experiments that image Bose-condensates based on the abovementioned principle. The superradiant scattering into end-fire-modes is seen to lead to non-trivial, time-dependent, spatial structure in both matter- and photon fields. The microscopic quantum fluctuations that trigger the initial superradiant dynamics lead to macroscopic fluctuations and asymmetries in the spatial features of absorption images during later stages. The modeled absorption profiles are in good qualitative agreement with experimental observations, confirming that superradiant scattering can be used to probe the condensed phase of a BEC at finite temperature while remaining insensitive to the non-condensed phase.

### Acknowledgments

We thank D. Stamper-Kurn for making his experimental results available prior to publication, and D. Meiser for countless useful discussions on this work.

This work is supported in part by the US Army Research Office, NASA, the National Science Foundation and the US Office of Naval Research.

## APPENDIX A

The short-time expressions may be obtained by making an approximation of zero depletion for the laser field,  $\mathcal{E}_L \approx 1$ , and keeping only highest order terms in the equations of motion for the atomic fields and end-fire-modes,

$$\frac{d\Psi_0(\mathbf{r}, t)}{d\tau} \approx \frac{i}{(1 - i\gamma/\delta)} |\mathcal{E}_L|^2 \Psi_0 \quad (\text{A-1})$$

$$\frac{d\Psi_{\mathbf{k}}(\mathbf{r}, t)}{d\tau} \approx \frac{i}{(1 - i\gamma/\delta)} \mathcal{E}_{-\mathbf{k}}^* \mathcal{E}_L \Psi_0 \quad (\text{A-2})$$

$$\text{sign}(k) \frac{\partial \mathcal{E}_k}{\partial \zeta} \approx \frac{i\aleph}{(1 - i\gamma/\delta)} \Psi_{-k}^\dagger \mathcal{E}_L \Psi_0 \quad (\text{A-3})$$

Equation (A-1) may immediately be solved to give

$$\Psi_0(\tau) = \Psi_0^{(0)} e^{i\eta\tau} e^{-\nu\tau} \quad (\text{A-4})$$

where  $\eta = \frac{1}{(1+(\gamma/\delta)^2)}$ ,  $\nu = \frac{\gamma/\delta}{(1+(\gamma/\delta)^2)}$  and  $\Psi_0^{(0)}$  is the initial condensate wave function which is assumed to be of the form  $\Psi_0^{(0)} = \phi_\zeta \phi_{(\xi, \Upsilon)}$ . Here  $\Upsilon = y/L$  is the dimensionless length in the  $y$ -direction. We also assume that in the initial state the recoiling atomic modes have the same wavefunction as the condensate, but smaller in amplitude by a factor  $\beta \ll 1$ . At time  $\tau = 0$  the EFM field is, by direct integration of Eq. (A-3),

$$\begin{aligned} \text{sign}(k) \mathcal{E}_k(\zeta) &= \aleph(i\eta - \nu)\beta |\phi_{(\xi, \Upsilon)}|^2 \left( \int_{-\frac{1}{2}}^{\zeta} |\phi_{\zeta'}|^2 d\zeta' + \mathcal{E}_0 \right) \\ &= \aleph(i\eta - \nu)\beta |\phi_{(\xi, \Upsilon)}|^2 \Delta(\zeta)/\alpha, \end{aligned} \quad (\text{A-5})$$

where  $\mathcal{E}_0$  is chosen so that the boundary condition  $\mathcal{E}_{-k}(1/2) = 0$  is satisfied and

$$\Delta(\zeta) = \alpha \left( \int_{-\frac{1}{2}}^{\zeta} |\phi_{\zeta'}|^2 d\zeta' + \mathcal{E}_0 \right) \quad (\text{A-6})$$

where

$$\alpha = \frac{\aleph}{((1 + (\gamma/\delta)^2))} |\phi_{\xi, \Upsilon}|^2. \quad (\text{A-7})$$

Now substitute Eq. (A-4) into Eq. (A-3) and define  $\tilde{\mathcal{E}}_{-k}^* = \mathcal{E}_{-k}^* e^{i\eta\tau + \nu\tau}$ . Then upon taking the time derivative of Eq. (A-3) and substitution of Eq. (A-2) therein we find

$$\text{sign}(k) \frac{\partial^2 \tilde{\mathcal{E}}_{-k}^*}{\partial \tau \partial \zeta} = \alpha |\phi_\zeta|^2 \tilde{\mathcal{E}}_{-k}^* e^{-2\nu\tau}. \quad (\text{A-8})$$

To solve this differential equation we first treat the case of zero dissipation, *i.e.*  $\eta \rightarrow 1$  and  $\nu \rightarrow 0$ , using the method

of Laplace Transforms. Taking the Laplace transform with respect to time of Eq. (A-8) we obtain

$$s \frac{\mathcal{E}_{-k}^*(\zeta, s)}{\partial \zeta} - i\aleph\beta |\Psi_0^{(0)}|^2 = \alpha |\phi_\zeta|^2 \mathcal{E}_{-k}^*(\zeta, s), \quad (\text{A-9})$$

in which  $\mathcal{E}_{-k}^*(\zeta, s) = \mathcal{L}(\tilde{\mathcal{E}}_{-k}^*)$ . Equation (A-9) is a linear first order differential equation and may be solved by standard means. We find

$$\mathcal{E}_{-k}^*(\zeta, s) = b e^{\Delta(\zeta)/s} - i\aleph\beta |\phi_{(\xi, \Upsilon)}|^2 / \alpha. \quad (\text{A-10})$$

The EFM field is found by inversion of the Laplace transform

$$\mathcal{E}_{-k}^*(\zeta, \tau) = \frac{1}{2\pi i} \int_{\mu-i\infty}^{\mu+i\infty} e^{s\tau} \mathcal{E}_{-k}^*(\zeta, s) ds. \quad (\text{A-11})$$

The contour of integration is chosen so as to include all poles of the integrand and the integral may be evaluated using the residue theorem. This is done by expanding both exponentials in the integrand in series and multiplying out the result. Integrating term-by-term the residue is found to be of the form

$$\sum_{n=1}^{\infty} \frac{\tau^{n-1} \Delta^n}{(n-1)! n!} = \sqrt{\frac{\Delta}{t}} I_1(2\sqrt{\tau\Delta}), \quad (\text{A-12})$$

where  $I_q$  is a modified Bessel function of the first kind of order  $q$ . Thus

$$\mathcal{E}_{-k}^*(\zeta, \tau) = i\beta \sqrt{\frac{\Delta}{\tau}} I_1(2\sqrt{\tau\Delta}) \Big|_{\nu=0}, \quad (\text{A-13})$$

and by substitution into Eq. (A-3)

$$\Psi_{\mathbf{k}}(\mathbf{r}, \tau) = \beta \Psi_0^{(0)} I_0(2\sqrt{\tau\Delta}) \Big|_{\nu=0}. \quad (\text{A-14})$$

We now turn to the case with non-zero dissipation. Since the solution to the latter must give rise to Eq. (A-13) for  $\nu \rightarrow 0$ , we suggest a solution of the form

$$\mathcal{E}_{-k}^* \sim a_1(\tau) \Delta + a_2(\tau) \Delta^2 + a_3(\tau) \Delta^3 + \dots \quad (\text{A-15})$$

where the  $a_n(\tau)$  are time dependent coefficients that must vanish at  $\tau = 0$  and reduce to  $\frac{\tau^{n-1}}{(n-1)! n!}$  for  $\nu \rightarrow 0$ . Substituting Eq. (A-15) into Eq. (A-8) one obtains a recursion relation for the  $n$ th coefficient

$$\frac{\partial a_n}{\partial \tau} = \frac{a_{n-1}}{n} e^{-2\nu\tau}. \quad (\text{A-16})$$

To satisfy the  $\nu \rightarrow 0$  condition we find that

$$a_n = \frac{1}{2^{n-1} \nu^{n-1} (n-1)! n!} (1 - e^{-2\nu\tau}). \quad (\text{A-17})$$

The latter leads to the desired solutions

$$\tilde{\mathcal{E}}_{-k}^*(\mathbf{r}, \tau) = i\beta (1 - i\gamma/\delta) \left( \frac{2\nu\Delta(\zeta)}{1 - e^{-2\nu\tau}} \right)^{\frac{1}{2}} I_1(g(\zeta)), \quad (\text{A-18})$$

and

$$\Psi_k(\mathbf{r}, \tau) = \beta \Psi_0^{(0)} I_0(g(\zeta)). \quad (\text{A-19})$$

The argument of the Bessel functions is given by

$$g(\zeta) = \left( \frac{2\Delta(\zeta)(1 - e^{-2\nu\tau})}{\nu} \right)^{\frac{1}{2}}. \quad (\text{A-20})$$

Finally, to find absorption profiles of the laser field we

have to include all terms in the differential equation

$$\frac{\partial \mathcal{E}_L}{\partial \xi} = \frac{i\aleph}{(1 - i\gamma/\delta)} \Psi_0^\dagger \left\{ \mathcal{E}_L \Psi_0 + \sum_k \mathcal{E}_k \Psi_{-k} \right\}. \quad (\text{A-21})$$

For simplicity we take a uniform distribution in the  $\xi$ -direction since the exact  $\xi$ -profile should not be too important in the short time limit. Substituting the short-time solutions obtained above we find

$$\mathcal{E}_L(\zeta) = e^{f(\zeta)} - \sum_{\sigma=\pm 1} \aleph \beta |\Psi_0^{(0)}|^2 \frac{(1 + i\gamma/\delta)}{(1 - i\gamma/\delta)} \frac{2\Delta(\zeta)}{g(\sigma\zeta)} I_1(g(\sigma\zeta)) I_0(g(\sigma\zeta)) \frac{e^{f(\zeta)} - 1}{f(\zeta)}, \quad (\text{A-22})$$

where

$$f(\zeta) = \aleph (i\eta - \nu) \phi_\zeta \int_{-\frac{\nu}{2L}}^{\frac{\nu}{2L}} \phi_{(\xi, \tau)} d\xi. \quad (\text{A-23})$$

For a Thomas-Fermi profile  $\phi_\zeta = \sqrt{(1/2)^2 - \zeta^2}$  and

$$\Delta(\zeta) = \alpha \left( \frac{2}{3}(1/2)^3 - (1/2)^2 \zeta + \frac{1}{3} \zeta^3 \right). \quad (\text{A-24})$$

- 
- [1] L. E. Sadler, J. M. Higbie, S. R. Leslie, M. Vengalattore, and D. M. Stamper-Kurn, arXiv:cond-mat/0609007 v1 (2005), private communication.
  - [2] M. Gross and S. Haroche, Phys. Rep. **93**, 301 (1982).
  - [3] R. H. Dicke, Phys. Rev. **93**, 99 (1954).
  - [4] S. Inouye, A. P. Chikkatur, D. M. Stamper-Kurn, J. Stenger, D. E. Pritchard, and W. Ketterle, Science **285**, 571 (1999).
  - [5] S. Inouye, T. Pfau, S. Gupta, A. P. Chikkatur, A. Görlitz, D. E. Pritchard, and W. Ketterle, Nature **402**, 641 (1999).
  - [6] D. Schneble, Y. Torii, M. Boyd, E. W. Streed, D. E. Pritchard, and W. Ketterle, Science **300**, 475 (2003).
  - [7] D. Schneble, K. C. Gretchen, W. S. Erik, B. Micah, D. E. Pritchard, and W. Ketterle, Phys. Rev. A **69**, 041601(R) (2004).
  - [8] Y. Yoshikawa, T. Sugiura, Y. Torii, and T. Kuga, Phys. Rev. A **69**, 041603(R) (2004).
  - [9] K. V. Krutitsky, F. Burgbacher, and J. Audretsch, Phys. Rev. A **59**, 1517 (1999).
  - [10] M. G. Moore and P. Meystre, Phys. Rev. Lett. **83**, 5202 (1999).
  - [11] O. E. Müstecaplıoglu and L. You, Phys. Rev. A **62**, 063615 (2000).
  - [12] M. M. Cola and N. Piovella, Phys. Rev. A **70**, 045601 (2004).
  - [13] F. Arecchi and E. Courtens, Phys. Rev. A **2**, 1730 (1970).
  - [14] R. Bonifacio, P. Schwendimann, and F. Haake, Phys. Rev. A **4**, 302 (1971).
  - [15] R. Bonifacio and L. Lugiato, Phys. Rev. A **11**, 1507 (1975).
  - [16] O. Zobay and G. M. Nikolopoulos, Phys. Rev. A **72**, 041604(R) (2005).
  - [17] O. Zobay and G. M. Nikolopoulos, Phys. Rev. A **73**, 013620 (2006).
  - [18] F. A. Hopf and P. Meystre, Physical Review A **12**, 2534 (1975).
  - [19] F. A. Hopf, P. Meystre, and D. W. McLaughlin, Physical Review A **13**, 777 (1976).
  - [20] F. Haake, J. W. Haus, H. King, G. Schröder, and R. Glauber, Phys. Rev. A **23**, 1322 (1981).
  - [21] I. E. Antoniou, V. V. Kocharovsky, V. L. V. Kocharovsky, Y. M. Mironov, and I. A. Shereshevsky, Computer Math. Applic. **34**, 751 (1997).
  - [22] F. E. van Dorselaer and G. Nienhuis, Phys. Rev. A **56**, 958 (1997).
  - [23] Y.B. Band, M. Trippenbach, J.P. Burke, and P.S. Julienne, Phys. Rev. Lett. **84**, 5462 (2000).
  - [24] D. M. Stamper-Kurn, L. E. Sadler, and M. Vengalattore (2006), private communication.
  - [25] H. Metcalf and P. van der Straten, *Laser cooling and Trapping* (Springer-Verlag New York Berlin Heidelberg, 2002).
  - [26] Around the center of the wavefunction this approximation has small corrections, second order in  $x_i x_j / r_i r_j$ , to the true Thomas-Fermi wavefunction.